Water Resources Research

RESEARCH ARTICLE
10.1029/2019WR026822

Special Section:
Advancing Process Representation in Hydrologic Models: Integrating New Concepts, Knowledge, and Data

A One-Dimensional Model for Turbulent Mixing in the Benthic Biolayer of Stream and Coastal Sediments

Stanley B. Grant[1,2], Jesus D. Gomez-Velez[3], Marco Ghisalberti[4], Ian Guymer[5], Fulvio Boano[6], Kevin Roche[7], and Judson Harvey[8]

[1]Occoquan Watershed Monitoring Laboratory, The Charles E. Via Jr. Department of Civil and Environmental Engineering, Virginia Tech, Manassas, VA, USA, [2]Center for Coastal Studies, Virginia Tech, Blacksburg, VA, USA, [3]Department of Civil and Environmental Engineering, Vanderbilt University, Nashville, TN, USA, [4]Oceans Graduate School, University of Western Australia, Perth, Western Australia, Australia, [5]Department of Civil and Structural Engineering, University of Sheffield, Sheffield, UK, [6]Department of Environment, Land and Infrastructure Engineering, Politecnico di Torino, Turin, Italy, [7]Department of Civil Engineering, Boise State University, Boise, ID, USA, [8]Earth System Processes Division, U.S. Geological Survey, Reston, VA, USA

Key Points:

- A one-dimensional diffusion model is developed and tested for dispersive mixing and turbulent diffusion in the benthic biolayer
- The model reproduces measurements of solute transfer into the sediment bed when diffusivity decays exponentially with depth
- The diffusivity increases with the permeability Reynolds number and decays over depths comparable to the benthic biolayer thickness

Supporting Information:

- Supporting Information S1
- Table S1

Correspondence to:
S. B. Grant,
stanleyg@vt.edu

Citation:
Grant, S. B., Gomez-Velez, J. D., Ghisalberti, M., Guymer, I., Boano, F., Roche, K., & Harvey, J. (2020). A one-dimensional model for turbulent mixing in the benthic biolayer of stream and coastal sediments. *Water Resources Research*, *56*, e2019WR026822. https://doi.org/10.1029/2019WR026822

Received 30 NOV 2019
Accepted 28 AUG 2020
Accepted article online 1 SEP 2020

Author Contributions:
Data curation: Ian Guymer
Methodology: Stanley B. Grant
Writing - original draft: Stanley B. Grant
Writing – review & editing: Stanley B. Grant, Jesus D. Gomez-Velez, Marco
(continued)

Abstract In this paper, we develop and validate a rigorous modeling framework, based on Duhamel's Theorem, for the unsteady one-dimensional vertical transport of a solute across a flat sediment-water interface (SWI) and through the benthic biolayer of a turbulent stream. The modeling framework is novel in capturing the two-way coupling between evolving solute concentrations above and below the SWI and in allowing for a depth-varying diffusivity. Three diffusivity profiles within the sediment (constant, exponentially decaying, and a hybrid model) are evaluated against an extensive set of previously published laboratory measurements of turbulent mass transfer across the SWI. The exponential diffusivity profile best represents experimental observations and its reference diffusivity scales with the permeability Reynolds number, a dimensionless measure of turbulence at the SWI. The depth over which turbulence-enhanced diffusivity decays is of the order of centimeters and comparable to the thickness of the benthic biolayer. Thus, turbulent mixing across the SWI may serve as a universal transport mechanism, supplying the nutrient and energy fluxes needed to sustain microbial growth, and nutrient processing, in the benthic biolayer of stream and coastal sediments.

Plain Language Summary How far and fast pollutants travel downstream is often conditioned on what happens in a thin veneer of biologically active bottom sediments called the benthic biolayer. However, before a pollutant can be removed in the benthic biolayer, it must first be transported across the sediment-water interface and through the interstitial fluids of these surficial sediments. In this paper we demonstrate that water column turbulence can play a key role in this process by transporting solutes into and out of the benthic biolayer of stream and coastal sediments.

1. Introduction

Many physical and biological processes in aquatic ecosystems depend on, or are strongly affected by, turbulent fluid motions at the sediment-water interface (SWI) (Franca & Brocchini, 2015; Grant, Azizian, et al., 2018). In streams, turbulence drives the vertical transport of dissolved constituents through the water column (Hondzo, 1998; O'Connor & Hondzo, 2008; Tomasek et al., 2018) governing the rate at which reactive constituents (e.g., nitrate) can be assimilated and removed by the streambed (Grant, Gomez-Velez, et al., 2018). Stream turbulence also enhances the transport of dissolved and fine particulate material through the benthic biolayer, the upper 5 cm of the streambed where much of the microbial biomass, as well as nutrient and pollutant processing, is concentrated (Battin et al., 2008; Caruso et al., 2017; Dahm et al., 2002; Harvey et al., 2013; Knapp et al., 2017; Tomasek et al., 2018; Trauth et al., 2014; Zarnetske et al., 2011).

Stream turbulence enhances mixing in the benthic biolayer in at least two ways (Figure 1a): (1) “dispersive mixing” occurs when turbulent eddies generate pressure waves that travel along the SWI and drive oscillating laminar flow across the interface (often called “turbulent pumping”; Boano et al., 2011; Higashino et al., 2009; Kim et al., 2020; Zhong et al., 2016); and (2) “turbulent diffusion” occurs when eddy motions

Ghisalberti, Ian Guymer, Fulvio Boano,
Kevin Roche, Judson Harvey

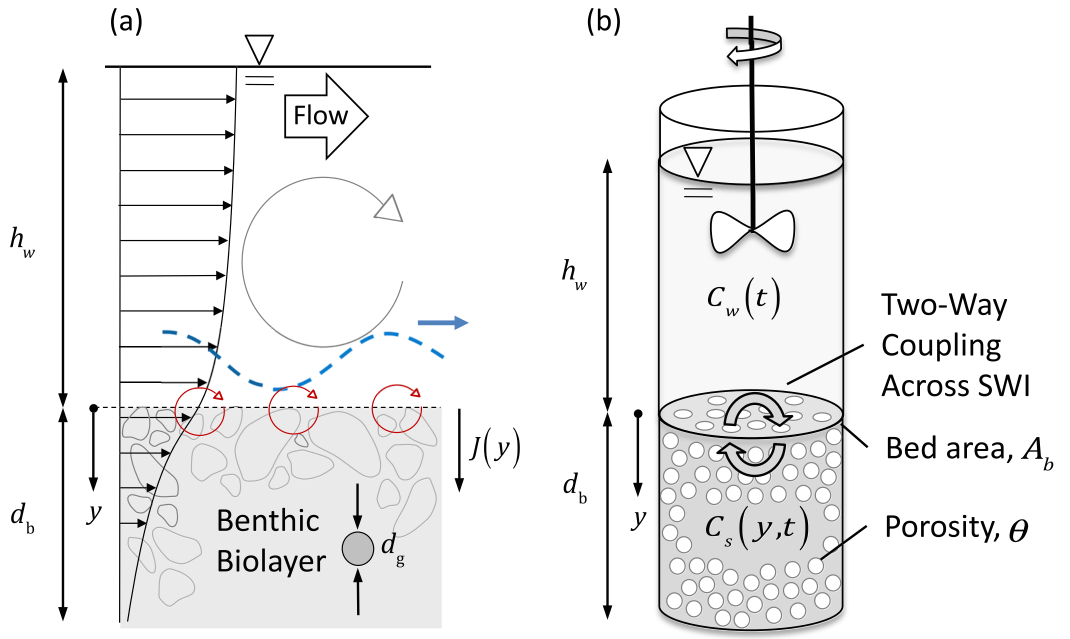

Figure 1. (a) An illustration of how water column turbulence can influence mass transport in the benthic biolayer. In this diagram, the benthic biolayer consists of a flat coarse-grained streambed subject to dispersive mixing and turbulent diffusion by a traveling pressure wave (dashed blue line), a mean velocity boundary layer that crosses the sediment-water interface (envelope of black arrows), and turbulence penetration (red eddies). The vertical mass flux $J(y)$ arising from these phenomena is assumed to follow the flux gradient model (Equation 1a). (b) Turbulent mass transport across the SWI can be measured in the laboratory using closed systems, such as a stirred tank. Two-way coupling across the SWI is indicated by the circular arrows.

penetrate the sediment and drive intermittent (advective) stirring of mass and momentum across the interface (Kim et al., 2020; Packman et al., 2004; Reidenbach et al., 2010; Roche et al., 2018; Voermans et al., 2017). Mathematically, dispersive mixing arises from spatial correlations between the time-averaged vertical velocity and the local mean solute concentration, while turbulent diffusion arises from temporal correlations between the turbulent vertical velocity component and the instantaneous concentration field (Voermans et al., 2018). If ripples and dunes are present on the streambed, mixing across the benthic biolayer is additionally facilitated by advective transport in upwelling and downwelling zones ("bedform pumping"; Azizian et al., 2017; Cardenas et al., 2008; Elliott & Brooks, 1997a, 1997b; Grant et al., 2014; Fleckenstein et al., 2010; Thibodeaux & Boyle, 1987) and the entrapment and release of interstitial fluids associated with bedform migration ("bedform turnover"; Elliot & Brooks, 1997a, 1997b; Wolke et al., 2020; Zheng et al., 2019). Solute mixing in the streambed is also controlled by molecular diffusion (which smooths out sharp concentration gradients generated by the above transport mechanisms; Hester et al., 2017) and biodiffusion (in which pore fluids and sediment are transported by benthic macrofauna and plants; Thibodeaux et al., 2011). The streambed's permeability and porosity fields, which vary temporally and spatially, can additionally influence mixing across the SWI (Herzog et al., 2018; Laube et al., 2018; Newcomer et al., 2016; Salehin et al., 2004; Stewardson et al., 2016).

Only under highly idealized conditions is it possible to resolve the spatially and temporally complex advection pathways generated by dispersive mixing and turbulent diffusion. Due to its simplicity, tractability, and consistency with scaling approaches, a common alternative is to describe mass transport across the SWI and through the benthic biolayer as a horizontally and temporally (over turbulence time scales) averaged flux gradient process (Voermans et al., 2018):

$$J(y,\ t) = -D_{\mathrm{eff}}(y)\frac{\partial(\theta C_s)}{\partial y} \tag{1a}$$

The variables $J(y,t)$ ($\mathrm{M\ L^{-2}\ T^{-1}}$) and $C_s(y,t)$ ($\mathrm{M\ L^{-3}}$) are the vertical solute flux and interstitial concentration at depth y (which is 0 at the SWI and increases with depth into the streambed, Figure 1a) and time

t in a sediment of porosity θ. The effective diffusivity for solute transport in the sediment, D_{eff} ($L^2\ T^{-1}$), encompasses contributions from (tortuosity-modified) molecular diffusion, D'_{m}, dispersive mixing, D_{d}, and turbulent diffusion, D_{t} (Boano et al., 2011, 2014; Chandler et al., 2016; Grant, Azizian, et al., 2018; Grant et al., 2012; Grant & Marusic, 2011; Nagaoka & Ohgaki, 1990; O'Connor & Harvey, 2008; O'Connor & Hondzo, 2008; Packman et al., 2004; Reidenbach et al., 2010; Richardson & Parr, 1988; Roche et al., 2018, 2019; Voermans et al., 2017, 2018; Zhong et al., 2016):

$$D_{\mathrm{eff}} = D'_m + D_d + D_t \tag{1b}$$

From refractive-index-matched particle image velocimetry (RIM-PIV) studies, Voermans et al. (2017) argued that the relative importance of the three terms in Equation 1b depends on the permeability Reynolds number, $Re_K = u_* \sqrt{K}/\upsilon$, a nondimensional number that incorporates the bed shear velocity u_* ($L\ T^{-1}$), sediment bed permeability K (L^2) and kinematic viscosity of water υ ($L^2\ T^{-1}$). Specifically, transport across the SWI is dominated by molecular diffusion at small values ($Re_K < 0.01$), dispersive mixing at intermediate values ($0.01 < Re_K < 2$), and turbulent diffusion at large values ($Re_K > 2$).

The use of Equations 1a and 1b to describe mixing in the benthic biolayer raises three questions. First, given that the mean and turbulent flow fields responsible for mixing across the benthic biolayer decrease with depth into the sediment (Breugem et al., 2006; Pokrajac & Manes, 2009; Roche et al., 2018; Voermans et al., 2017), what is the vertical structure of the effective diffusivity? Second, for a given vertical structure, how well does the flux gradient model (Equation 1a) describe solute transport through the streambed? Third, how do we extrapolate effective diffusivities measured in the laboratory to streams and coastal sediments? Here, we address these three questions in the context of dispersive mixing and turbulent diffusion across a flat sediment bed. Complementary efforts are underway to address mixing in the benthic biolayer by bedform pumping and bedform turnover (cf. Grant et al., 2020).

The paper is organized as follows. In section 2 we demonstrate, through the application of Duhamel's Theorem, that solute concentration in the interstitial fluids of the sediment bed can be represented as a convolution of solute concentration in the water column with the Green's function for mass transport in the streambed (Leij et al., 2000). This leads to a set of explicit solutions for the spatiotemporal evolution of concentrations in the water and sediment columns of a closed system. Notably, these solutions capture the two-way coupling of concentration evolution above and below the SWI, whereby mass transfer out of the streambed alters concentration in the overlying water column which, in turn, alters mass transfer into the streambed, and so on (Figure 1b). We then derive four Green's functions for two choices of the lower-boundary condition (finite or semi-infinite sediment domain) and three functional forms of the diffusivity profile. In section 3 we demonstrate how this theory can be used to simulate unsteady mass transfer in a closed system, and in section 4 apply it to previously published measurements of turbulent mass transfer across a flat unconsolidated sediment bed in a well-stirred tank. We address the three questions raised above in section 5 and present our conclusions in section 6.

2. Analytical Modeling Framework

2.1. Duhamel's Solution for Turbulent Mixing in the Benthic Biolayer

Averaging over the time scale of turbulence and assuming sediment porosity does not change appreciably through the benthic biolayer (Knapp et al., 2017), mass conservation for a conservative solute in a horizontally uniform system takes the form

$$\frac{\partial C_s}{\partial t} = \frac{\partial}{\partial y}\left(D_{\mathrm{eff}}(y)\frac{\partial C_s}{\partial y}\right). \tag{2a}$$

In this study, we investigate how mass transfer across the SWI is influenced by the variation in effective diffusivity with depth: $D_{\mathrm{eff}}(y) = D_{\mathrm{eff},0} f(y)$, where $D_{\mathrm{eff},0}$ is the effective diffusivity at the SWI (henceforth referred to as the surficial effective diffusivity) and $f(y)$ is a piecewise continuous function for which $f(0) = 1$. Adopting this functional form for the effective diffusivity, Equation 2a can be rewritten in dimensionless form where the new dependent variable, c_s (–), incorporates the solute's initial concentration in the sediment and water columns (C_{s0} and C_{w0}, respectively):

$$\frac{\partial c_s}{\partial \bar{t}} = \frac{\partial}{\partial \bar{y}}\left(f(\bar{y})\frac{\partial c_s}{\partial \bar{y}}\right) \tag{2b}$$

$$c_s(\bar{y}, \bar{t}) = \frac{C_s(\bar{y}, \bar{t}) - C_{s0}}{C_{w0} - C_{s0}},\ c_s(\bar{y}, \bar{t}) \in [0,\ 1] \tag{2c}$$

$$\bar{t} = t/t_{\mathrm{T}} \geq 0,\ t_{\mathrm{T}} = 1/\left(D_{\mathrm{eff},\,0}a^2\right),\quad \bar{y} = ay \geq 0. \tag{2d}$$

The constant a (L^{-1}) is an inverse depth scale (whose definition will be shown to depend on the choice of diffusivity profile) and t_{T} is a time constant for solute mixing in the benthic biolayer. Given the definition of dimensionless concentration (Equation 2c), the initial condition for Equation 2b becomes

$$c_s(\bar{y}, \bar{t} = 0) = 0 \tag{3a}$$

At the upper boundary (the SWI, $y = 0$) we require that the interstitial solute concentration equals the solute concentration in the overlying well-mixed water column, $C_s(y = 0, t) = C_w(t)$. Expressed in dimensionless form the upper boundary condition becomes

$$c_s(\bar{y} = 0,\ \bar{t}) = \frac{C_w(\bar{t}) - C_{s0}}{C_{w0} - C_{s0}}H(\bar{t}) = c_w(\bar{t})H(\bar{t}) \tag{3b}$$

$$c_w(\bar{t}) = \frac{C_w(\bar{t}) - C_{s0}}{C_{w0} - C_{s0}},\ c_w(\bar{t}) \in [0,\ 1],\quad H(\bar{t}) = \{\,0;\ \bar{t}\ \leq 1,\ \bar{t} > 0 \tag{3c}$$

The Heaviside step function $H(\bar{t})$ (–) in Equation 3b ensures the upper boundary condition is 0 for $\bar{t} \leq 0$ (this detail becomes important for the application of Duhamel's Theorem below). Expression of the upper boundary condition in this way implies that mass transfer across the SWI is limited by the transport of solute within the streambed and not by mixing across the overlying concentration boundary layer (Grant, Azizian, et al., 2018; Grant, Gomez-Velez, et al., 2018). That is, the Biot number (the ratio of time scales for diffusive mixing in the streambed and mass transfer across the concentration boundary layer) is much greater than unity (Incropera et al., 2007).

One of two lower-boundary conditions can be selected, depending on whether the sediment bed is finite (Equation 3d) or semi-infinite (Equation 3e) in extent.

$$\left.\frac{\partial c_s}{\partial \bar{y}}\right|_{\bar{y}=\bar{d}_b} = 0 \tag{3d}$$

$$c_s(\bar{y}\rightarrow\infty, \bar{t}) = 0 \tag{3e}$$

Equation 3d enforces a no-flux boundary condition at the normalized depth $\bar{d}_b = ad_b$ (–) where d_b is the depth of the sediment bed (Figure 1). Equation 3e prescribes that, deep within the bed ($\bar{y}\rightarrow\infty$), the interstitial concentration is maintained at its initial value.

As documented in the supporting information (Texts S1 and S2), by invoking Duhamel's Theorem (Perez Guerrero et al., 2013) the above system of equations can be solved for any time-varying solute concentration in the overlying water column, any piecewise continuous diffusivity profile, and either a finite or semi-infinite streambed. The solution is a convolution of the dimensionless water column concentration, $c_w(\bar{t})$, with a so-called Green's function (Leij et al., 2000; Myers, 1971), $G(\bar{y}, \bar{t})$ (T^{-1}), scaled here by the mixing time scale introduced earlier (Equation 2d), $\overline{G}(\bar{y}, \bar{t}) = t_{\mathrm{T}}G(\bar{y}, \bar{t})$:

$$c_s(\bar{y}, \bar{t}) = \int_0^{\bar{t}} \overline{G}(\bar{y}, v)c_w(\bar{t} - v)dv \tag{4}$$

According to Equation 4, dimensionless solute concentration in the interstitial fluid at any depth and time, $c_s(\bar{y}, \bar{t})$, depends on the entire prior history of dimensionless solute concentration in the water column, $c_w(\bar{t})$, filtered through the Green's function, $\overline{G}(\bar{y}, \bar{t})$. Green's function, in turn, is a fundamental solution to the diffusion equation (Equation 2b) that characterizes the response of solute concentration in the interstitial fluid of the streambed to an impulsive injection of mass at the SWI at $\bar{t} = 0$, $c_w(\bar{t}) = \delta(\bar{t})$, where $\delta(\bar{t})$ (–) is the Dirac delta function. The mathematical form of the Green's function depends on the vertical structure of the diffusivity profile, $f(\bar{y})$, and the lower-boundary condition (either Equation 3d or 3e). Four Green's functions, corresponding to different combinations of the diffusivity profile and lower-boundary condition, are derived in section 2.3.

2.2. Two-Way Coupling Across the SWI in a Closed System

In typical applications of Duhamel's Theorem, the functional form of the non-homogeneous boundary condition (i.e., the water column concentration, $c_w(\bar{t})$) is stipulated in advance. In our case, however, the water and sediment concentrations are fully coupled through mass flux across the SWI. For a closed system, like the stirred tank illustrated in Figure 1b, the change of solute mass in the water column is equal to the rate of mass transfer across the SWI by dispersive mixing and turbulent diffusion:

$$A_b h_w \frac{dC_w}{dt} = A_b \theta D_{\mathrm{eff},\,0} \left.\frac{\partial C_s}{\partial y}\right|_{y=0,\,t} \tag{5a}$$

New variables appearing here include the interfacial area, A_b, of the streambed and the height of the water column, h_w. The streambed porosity, $0 < \theta < 1$, appears on the righthand side of Equation 5a to capture the abrupt change in area over which mass transport occurs above and below the SWI (Grant et al., 2012). Using the dimensionless variables introduced earlier, Equation 5a can be expressed as follows where the new dimensionless variable, $\bar{h}_w$ (Equation 5c), is a scaled form of the water column depth:

$$\frac{dc_w}{d\bar{t}} = \frac{1}{\bar{h}_w} \left.\frac{\partial c_s}{\partial \bar{y}}\right|_{\bar{y}=0,\,\bar{t}} \tag{5b}$$

$$\bar{h}_w = \frac{a h_w}{\theta} \tag{5c}$$

Two-way coupling across the SWI manifests mathematically as a dependence of concentration in the water column (left-hand side [LHS]; Equation 5b) on concentration in the sediment (right-hand side [RHS]; Equation 5b) and, simultaneously, the dependence of concentration in the sediment (LHS, Equation 4) on concentration in the water column (through its convolution with Green's function, RHS, Equation 4). This two-way coupling can be solved exactly by manipulating the water and sediment mass balance equations in the Laplace domain. As demonstrated in the supporting information (Text S3), the result is a set of fully coupled solutions for solute concentration in the water and sediment columns of a closed system:

$$C_w(\bar{t}) = (C_{w0} - C_{s0})\mathcal{L}^{-1}\left[\frac{1/\bar{s}}{1 - \frac{1}{\bar{s}\bar{h}_w}\left(\partial\widetilde{G}/\partial\bar{y}\right)_{\bar{y}=0,\,\bar{s}}}\right] + C_{s0} \tag{6a}$$

$$C_s(\bar{y},\bar{t}) = (C_{w0} - C_{s0})\mathcal{L}^{-1}\left[\frac{\widetilde{G}(\bar{y},\bar{s})/\bar{s}}{1 - \frac{1}{\bar{s}\bar{h}_w}\left(\partial\widetilde{G}/\partial\bar{y}\right)_{\bar{y}=0,\,\bar{s}}}\right] + C_{s0} \tag{6b}$$

Here, $\mathcal{L}^{-1}[\cdot]$ represents the inverse Laplace transform, $\bar{s} = st_{\mathrm{T}}$ (–) is a dimensionless form of the Laplace transform variable s (T^{-1}), and $\widetilde{G}$ is the Laplace transform of the dimensionless Green's function which, as noted earlier, depends on the diffusivity depth profile $f(\bar{y})$ and bottom boundary condition. A corresponding set of solutions can be derived without two-way coupling (whereby the diffusion equation's upper boundary condition is maintained at $C_s(\bar{y} = 0,\, \bar{t}) = C_{w0}$):

$$C_w(\bar{t}) = (C_{w0} - C_{s0})\mathcal{L}^{-1}\left[\frac{1}{\bar{s}}\left(\frac{1}{\bar{s}\bar{h}_w}\left.\frac{\partial\widetilde{G}}{\partial\bar{y}}\right|_{\bar{y}=0,\,\bar{s}} + 1\right)\right] + C_{s0} \tag{6c}$$

$$C_s(\bar{y},\bar{t}) = (C_{w0} - C_{s0})\mathcal{L}^{-1}\left[\frac{\widetilde{G}(\bar{y},\bar{s})}{\bar{s}}\right] + C_{s0} \tag{6d}$$

The inverse Laplace transforms in Equations 6a–6d were determined analytically or evaluated numerically using Gaussian quadrature (Graf, 2004).

2.3. Laplace Domain Solutions for the Green's Function

In Table 1 we present four Laplace domain solutions for the Green's function given three choices of diffusivity depth profile and two choices of bottom boundary condition (finite or semi-infinite sediment bed) (derivations in the supporting information, Text S4). This analysis therefore provides 16 different solution combinations for concentration in the water and sediment columns of a closed system with (Equations 6a and 6b) or without (Equations 6c and 6d) two-way coupling across the SWI.

The three diffusivity depth profiles evaluated are (Figure 2): (1) constant (C Profile, Equation 7a); (2) exponentially decaying (E Profile, Equation 7b); and (3) constant to exponentially decaying diffusivity (C2E Profile, Equation 7c).

$$f_{\mathrm{C}}(\overline{y}) = 1, \quad \overline{y} = a_{\mathrm{C}} y \tag{7a}$$

$$f_{\mathrm{E}}(\overline{y}) = e^{-\overline{y}}, \quad \overline{y} = a_{\mathrm{E}} y \tag{7b}$$

$$f_{C2E}(\overline{y}) = \begin{cases} 1, \; 0 \le \overline{y} \le \overline{\ell}_{\mathrm{t}} \\ e^{-\left(\overline{y} - \overline{\ell}_{\mathrm{t}}\right)}, \; \overline{y} > \overline{\ell}_{\mathrm{t}} \end{cases}, \quad \overline{\ell}_t = a_{\mathrm{C2E}} \ell_t, \quad \overline{y} = a_{\mathrm{C2E}} y \tag{7c}$$

Most laboratory (Grant et al., 2012; Marion & Zaramella, 2015; O'Connor & Harvey, 2008) and field (Wörman, 2000) studies of mixing across the SWI adopt the C Profile. However, several studies (Chandler et al., 2016; Nagaoka & Ohgaki, 1990; Roche et al., 2019) have shown that turbulent mixing in the sediment bed decays exponentially with depth, and a recent numerical modeling study concluded that the E Profile is consistent with experimental breakthrough curves measured in the laboratory and field (Bottacin-Busolin, 2019). The C2E Profile captures enhanced mixing at the top of the streambed by extending the surficial effective diffusivity $D_{\mathrm{eff},0}^{\mathrm{C2E}}$ to a depth $y = \ell_t$ (L) below the SWI (c.f., the analytical model in Roche et al., 2019). The diffusivity profile declines exponentially below this depth, $y > \ell_t$. The dimensionless form of the enhanced mixing depth is defined as follows, $\overline{\ell}_t = a_{\mathrm{C2E}} \ell_t$.

3. Example of the Theory's Application to Mixing Across the SWI in a Stirred Tank

Consider an experiment similar to those described in section 4, in which mass M of a conservative solute is added to the interstitial fluid of the sediment bed in an otherwise solute-free stirred tank. Adopting the notation from Figure 1b, the initial interstitial concentration is $C_{s0} = M/(d_b A_b \theta)$. At time $t = 0$ the impeller is turned on, causing the concentration in the overlying water column to rise as solute is turbulently mixed out of the bed. Over time, the water and sediment concentrations will approach a final (well-mixed) equilibrium concentration, C_{eq}:

$$\frac{C_{eq}}{C_{s0}} = \frac{\overline{d}_b}{1 + \overline{d}_b}, \; \overline{d}_b = d_b \theta / h_w \tag{8a}$$

Within the context of our modeling framework, the temporal evolution of solute concentration from its initial (all solute mass in the sediment) to final (well-mixed) state depends on the diffusivity's depth profile, whether two-way coupling across the SWI is considered and whether the sediment bed is modeled as semi-infinite or finite.

If we adopt the C Profile, for example, the theory presented in section 2 leads to the following three solutions for solute concentration in the water column (Text S5): (1) a “null model” for an infinitely deep sediment bed without two-way coupling (Equation 8b); (2) an “infinite bed” model for an infinite sediment bed with two-way coupling (Equation 8c); and (3) a “finite bed” model for a finite sediment bed with two-way coupling (Equation 8d).

Table 1
Green's Functions for Various Choices of the Diffusivity Depth Profile and Sediment Bed Extent (Finite or Semi-Infinite)

C Profile, $f_{\mathrm{C}}(\bar{y}) = 1$

Semi-infinite sediment bed, $\bar{y} = a_{\mathrm{C}} y > 0,\ \bar{s} = s t_{\mathrm{T}}$

$$\widetilde{G}(\bar{y}, \bar{s}) = e^{-\bar{y}\sqrt{\bar{s}}},\ \bar{y} > 0 \quad \text{(T1)}$$

Finite sediment bed, $\bar{y} = a_{\mathrm{C}} y > 0,\ \bar{d}_b = d_b a_{\mathrm{C}} > 0,\ \bar{y} < \bar{d}_b,\ \bar{s} = s t_{\mathrm{T}}$

$$\widetilde{G}(\bar{y}, \bar{s}) = \frac{e^{-\bar{y}\sqrt{\bar{s}}}\left(e^{2\bar{d}_{\mathrm{b}}\sqrt{\bar{s}}} + e^{2\bar{y}\sqrt{\bar{s}}}\right)}{1 + e^{2\bar{d}_{\mathrm{b}}\sqrt{\bar{s}}}} \quad \text{(T2)}$$

E Profile, $f_{\mathrm{E}}(\bar{y}) = e^{-\bar{y}}$

Semi-infinite sediment bed, $\bar{y} = a_{\mathrm{E}} y > 0,\ \bar{s} = s t_{\mathrm{T}}$

$$\widetilde{G}(\bar{y}, \bar{s}) = \sqrt{e^{\bar{y}}}\frac{K_1\left(2\sqrt{\bar{s}e^{\bar{y}}}\right)}{K_1\left(2\sqrt{\bar{s}}\right)} \quad \text{(T3)}$$

$$\text{C2E Profile, } f_{\mathrm{C2E}}(\bar{y}) = \begin{cases} 1,\ 0 \le \bar{y} \le \bar{\ell}_t \\ e^{-\bar{y}},\ \bar{y} > \bar{\ell}_t \end{cases}$$

Semi-infinite sediment bed, $\bar{y} = a_{\mathrm{C2E}} y > 0,\ \bar{\ell}_t = a_{\mathrm{C2E}} \ell_t > 0,\ \bar{s} = s t_{\mathrm{T}}$

$$\widetilde{G}(\bar{y}, \bar{s}) = \begin{cases} \widetilde{G}_1(\bar{y}, \bar{s}),\ \bar{y} \le \bar{\ell}_{\mathrm{t}} \\ \widetilde{G}_2(\bar{y}, \bar{s}),\ \bar{y} > \bar{\ell}_{\mathrm{t}}. \end{cases} \quad \text{(T4a)}$$

$$\widetilde{G}_1(\bar{y}, \bar{s}) = \frac{K_1\left(2\sqrt{\bar{s}}\right)\cosh\left[\sqrt{\bar{s}}\left(\bar{y} - \bar{\ell}_{\mathrm{t}}\right)\right] - K_0\left(2\sqrt{\bar{s}}\right)\sinh\left[\sqrt{\bar{s}}\left(\bar{y} - \bar{\ell}_{\mathrm{t}}\right)\right]}{K_1\left(2\sqrt{\bar{s}}\right)\cosh\left(\bar{\ell}_{\mathrm{t}}\sqrt{\bar{s}}\right) + K_0\left(2\sqrt{\bar{s}}\right)\sinh\left(\bar{\ell}_{\mathrm{t}}\sqrt{\bar{s}}\right)} \quad \text{(T4b)}$$

$$\widetilde{G}_2(\bar{y}, \bar{s}) = \frac{e^{(\bar{y} - \bar{\ell}_{\mathrm{t}})/2} K_1\left(2e^{(\bar{y} - \bar{\ell}_{\mathrm{t}})/2}\sqrt{\bar{s}}\right)}{K_1\left(2\sqrt{\bar{s}}\right)\cosh\left(\bar{\ell}_{\mathrm{t}}\sqrt{\bar{s}}\right) + K_0\left(2\sqrt{\bar{s}}\right)\sinh\left(\bar{\ell}_{\mathrm{t}}\sqrt{\bar{s}}\right)} \quad \text{(T4c)}$$

Note. The functions K_0, K_1, and K_2 are modified Bessel functions of the second kind.

$$\frac{C^{\mathrm{C}}_{w,\,\mathrm{null}}(\bar{t}_{\mathrm{C}})}{C_{s0}} = 2\sqrt{\frac{\bar{t}_{\mathrm{C}}}{\pi}}, \quad \bar{t}_{\mathrm{C}} = \theta^2 D^{\mathrm{C}}_{\mathrm{eff},\,0} t / h_w^2, \tag{8b}$$

$$\frac{C^{\mathrm{C}}_{w,\,\infty}(\bar{t}_{\mathrm{C}})}{C_{s0}} = 1 - e^{\bar{t}_{\mathrm{C}}}\mathrm{erfc}\left(\sqrt{\bar{t}_{\mathrm{C}}}\right) \tag{8c}$$

$$\frac{C^{\mathrm{C}}_{w,\,\mathrm{finite}}(\bar{t}_{\mathrm{C}})}{C_{s0}} = 1 - \mathcal{L}^{-1}\left[\frac{1/\bar{s}}{1 + \tanh\left(\bar{d}_b\sqrt{\bar{s}}\right)/\sqrt{\bar{s}}}\right] \tag{8d}$$

The concentration in the water column is unbounded for the null and infinite bed models, because their lower-boundary condition implies that an infinite mass of solute is stored in the sediments. The superscript “C” indicates the solutions are specific to the C Profile. The corresponding set of solutions for interstitial concentration in the sediment bed are as follows:

$$\frac{C^{\mathrm{C}}_{s,\,\mathrm{null}}(\bar{y}_{\mathrm{C}}, \bar{t}_{\mathrm{C}})}{C_{s0}} = \mathrm{erfc}\left(\frac{\bar{y}_{\mathrm{C}}}{\sqrt{4\bar{t}_{\mathrm{C}}}}\right), \quad \bar{y}_{\mathrm{C}} = \theta y / h_w \tag{9a}$$

$$\frac{C^{\mathrm{C}}_{s,\,\infty}(\bar{y}_{\mathrm{C}}, \bar{t}_{\mathrm{C}})}{C_{s0}} = 1 - e^{\bar{t}_{\mathrm{C}}} + \bar{y}_{\mathrm{C}}\mathrm{erfc}\left(\frac{2\bar{t}_{\mathrm{C}} + \bar{y}_{\mathrm{C}}}{\sqrt{4\bar{t}_{\mathrm{C}}}}\right) \tag{9b}$$

$$\frac{C^{\mathrm{C}}_{s,\,\mathrm{finite}}(\bar{y}_{\mathrm{C}}, \bar{t}_{\mathrm{C}})}{C_{s0}} = 1 - \mathcal{L}^{-1}\left[\frac{\cosh\left(\left(\bar{d}_b - \bar{y}_{\mathrm{C}}\right)\sqrt{\bar{s}}\right)}{\bar{s}\cosh\left(\bar{d}_b\sqrt{\bar{s}}\right) + \sqrt{\bar{s}}\sinh\left(\bar{d}_b\sqrt{\bar{s}}\right)}\right] \tag{9c}$$

The null model predicts that concentration in the water column increases unboundedly with the square root of time (Figure 3a). Concentration in the infinite bed model rises with the null model initially (until $\sqrt{\bar{t}_{\mathrm{C}}} = 0.25$) but slows as two-way coupling reduces mass transfer across the SWI. The finite bed model exhibits three phases: tracking the null model early on, transitioning to the infinite bed model at intermediate times, and eventually stabilizing at the final equilibrium concentration.

Similar patterns are evident for model-predicted concentration in the sediment (Figure 3b). Here we focus on the evolution of interstitial solute concentration in the upper portion of the bed, $\bar{y}_{\mathrm{C}} = 0.05$. The null model

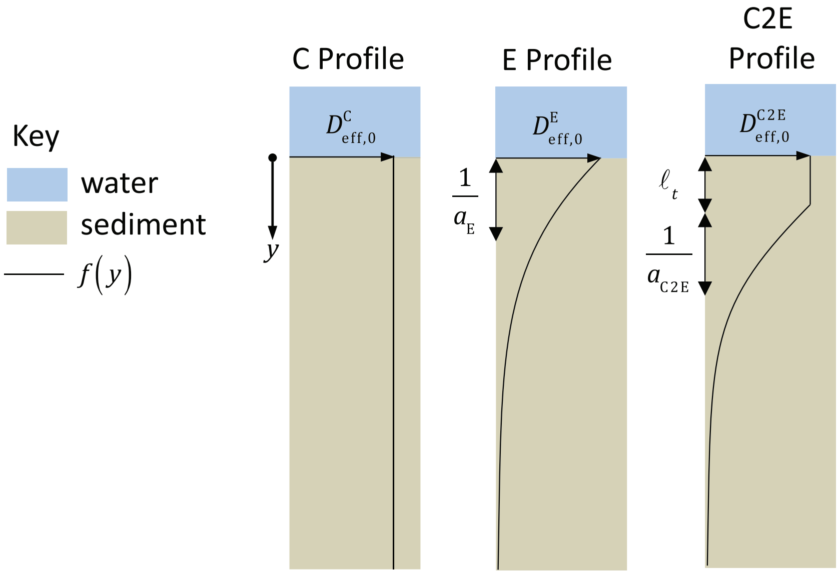

Figure 2. Three functional forms of the effective diffusivity profile $f(y)$ trialed in this study (Equations 7a–7c). Variables represent the depth into the sediment bed (y), surficial effective diffusivity (at the SWI, $D_{\mathrm{eff},0}$), a mixing depth scale ($1/a$), and the thickness of constant mixing at the surface of the sediment bed (ℓ_t).

predicts a rapid decrease in concentration initially (as solute in the upper portion of the streambed mixes into the water column) followed by a gradual decline over time (as solute from deeper in the bed mixes upward). The infinite bed solution declines with the null model initially, then rebounds as two-way coupling slows mass transfer across the SWI. The finite bed model exhibits the same three phases as in the water column, tracking the null model at short times, following the infinite bed model at intermediate times, and eventually stabilizing at an equilibrium concentration.

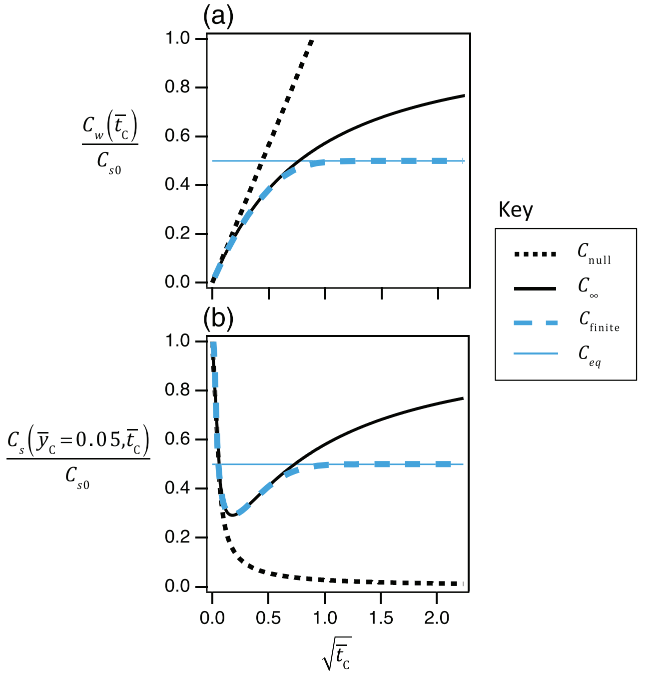

Figure 3. The influence of two-way coupling and finite bed depth on the evolution of solute concentration in the (a) water column and (b) interstitial fluids of the sediment bed, assuming solute is initially present only in the interstitial fluids of the sediment bed and the diffusivity profile is constant with depth (C Profile). The normalized bed depth was set to unity for these simulations, $\bar{d}_b = 1$.

4. Applying the Theory to Previously Published Measurements

4.1. Experiments of Chandler Et Al. (2016)

The theoretical framework above was applied to an extensive set of previously published measurements of turbulent mixing of a conservative tracer (Rhodamine WT) across a flat SWI in a stirred tank (Chandler et al., 2016; "C16" henceforth). C16's experiments are notable because they (1) covered a range of bed shear velocities (u_*= 0.01–0.04 m s^{-1}), mean grain diameters (d_g= 0.15–5.00 mm), and sediment permeabilities (K= 0.18–223 × 10^{-10} m^2); and (2) simultaneously measured water and sediment column concentrations. The second feature permits a direct comparison of mixing parameters estimated from concentration data collected exclusively above or below the SWI.

C16's experimental methods, and the approach we used for parameter estimation and model performance evaluation, are briefly described here (see Text S6 for details). The sediment column consisted of randomly packed single-sized spherical glass spheres, with a depth d_b= 0.2 m and a porosity θ= 0.38–0.39. In all experiments, the initial state was a Rhodamine WT saturated sediment bed ($C_{s0}\approx$ 100 ppb) and a Rhodamine WT-free water column ($C_{w0}\approx$ 0 ppb) (Table S1). Tracer concentrations were monitored fluorometrically in the water column and at five depths in the sediment column (y = 0.015, 0.049, 0.083, 0.117, 0.151 m) at 0.1 Hz over a period of hours to days. Diffusivity profile parameters were inferred by minimizing the root-mean-square error (RMSE) in nonlinear least squares regression between experimental data and model predictions. The corrected Akaike Information Criterion (AICc), which accounts for the trade-off between model fit and model complexity, was used to rank the performance of the three diffusivity profiles; the top-ranked model has the smallest AICc value (Aho et al., 2014). For model fitting, we used the "infinite bed" model specific to each profile and restricted the experimental time window to periods when Rhodamine WT concentration at the deepest sensor changed by <10% (Table S1). Parameter values for all three diffusivity profiles (C, E, C2E) were inferred from the water column data measured in 20 of C16's experiments (Tables S2, S3, and S5); six experiments were excluded due to missing data or other issues. E Profile parameters were separately estimated from sediment column data measured in the same 20 experiments (Table S4).

4.2. Experimental Evaluation of the C Profile

In comparison to C16's experimental data, there is significant bias in the concentrations predicted by the C Profile's infinite bed model (Figure 4a). In this figure, normalized Rhodamine WT measurements are plotted against the square root of dimensionless time, $\sqrt{\bar{t}_C} = \sqrt{t/t_C}$. The time constant, $t_C = h_w^2/\left(\theta^2 D^{C}_{\mathrm{eff},0}\right)$, varies by experiment depending on the inferred value of the effective diffusivity (Table S2); the other two parameters, h_w and θ, vary negligibly. Thus, C16's data can be compared directly to a single model prediction for the time evolution of concentration in the water column (Equation 8c, upper graph in Figure 4a) and at two depths (15 and 151 mm) in the sediment column (Equation 9b, lower graph in Figure 4a). For clarity, measured Rhodamine WT concentrations at the three intermediate depths (4.9, 8.3, 11.7 cm) are not included in this figure;

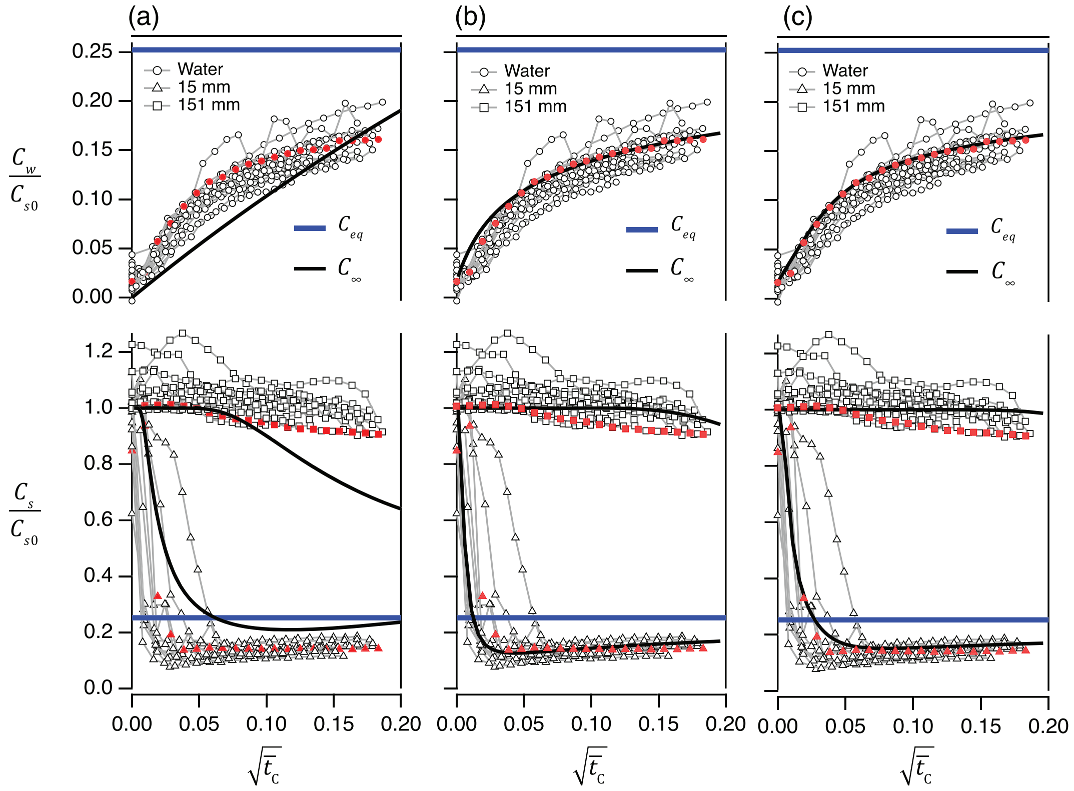

Figure 4. Chandler et al.'s water (top graphs) and sediment (bottom graphs) column measurements of Rhodamine WT (points) compared to infinite bed model predictions for the (a) C Profile, (b) E Profile, and (c) C2E Profile. Black curves and red data points are model-predicted and measured solute concentration, respectively, in the water column (top graph) and at two depths in the sediment bed (15 and 151 mm below the SWI, lower graph) of C16's Exp ID# 20110613. Blue horizontal lines represent the well-mixed (equilibrium) concentration (Equation 8a).

In C16's experiments, the concentration of Rhodamine WT in the water column is proportional to the cumulative mass of Rhodamine WT transferred from the sediment to the water column up to that point in time. Thus, the C Profile model underestimates and overestimates mass transfer out of the sediment bed at short and long times, respectively (Figure 4a, upper graph). The underlying problem can be diagnosed by comparing model-generated and measured Rhodamine WT concentrations in the sediment bed (lower graph, Figure 4a). The C Profile model underestimates mixing in the surficial portion of the bed at short times (predicted concentrations exceed measured concentrations at 15 mm) and overestimates mixing deeper in the bed at later times (predicted concentrations less than measured concentrations at 151 mm).

4.3. Experimental Evaluation of the E Profile

Model bias is reduced substantially when the effective diffusivity decays exponentially with depth (Figure 4b). The E Profile's infinite bed model was constructed by substituting its Green's function (Equation T3 in Table 1) into the water and sediment solutions for a closed system with two-way coupling (Equations 6a and 6b):

$$C^{E}_{w,\infty}(\bar{t}_{\mathrm{E}}) = (C_{w0}-C_{s0})\mathcal{L}^{-1}\left[\frac{\bar{h}_w K_1\left(2\sqrt{\bar{s}}\right)}{\bar{s}\bar{h}_w K_1\left(2\sqrt{\bar{s}}\right)+\sqrt{\bar{s}}K_0\left(2\sqrt{\bar{s}}\right)}\right]+C_{s0} \tag{10a}$$

$$C^{E}_{s,\infty}(\bar{y},\bar{t}_{\mathrm{E}}) = (C_{w0}-C_{s0})\mathcal{L}^{-1}\left[\frac{\bar{h}_w \sqrt{e^{\bar{y}}}K_1\left(2\sqrt{e^{\bar{y}}\bar{s}}\right)}{\bar{s}\bar{h}_w K_1\left(2\sqrt{\bar{s}}\right)+\sqrt{\bar{s}}K_0\left(2\sqrt{\bar{s}}\right)}\right]+C_{s0} \tag{10b}$$

$$\bar{t}_\mathrm{E} = t/t_\mathrm{E}, \quad t_\mathrm{E} = 1/\left(a_\mathrm{E}^2 D_{\mathrm{eff},\,0}^\mathrm{E}\right), \quad \bar{h}_w = a_\mathrm{E} h_w/\theta, \quad \bar{y} = a_\mathrm{E} y \tag{10c}$$

The superscript or subscript "E" indicates that these solutions are specific to the E Profile. Because the E Profile model has two unknown parameters ($D_{\mathrm{eff},\,0}^\mathrm{E}$ and a_E), there is no longer a single curve against which all of C16's data can be compared (as was the case for the C Profile in Figure 4a). For the E Profile (and C2E Profile described below) model-data comparisons must be conducted on an experiment-by-experiment basis. In Figure 4b the comparison is performed for a typical C16 experiment (ID #20110613, red points in the figure). The E Profile infinite bed model reproduces water column measurements of Rhodamine WT concentration (top graph, Figure 4b), although some bias is evident for $\sqrt{\bar{t}_\mathrm{C}} < 0.05$. Sediment concentrations predicted by the E Profile's infinite bed model capture the fast and slow mixing out of the shallow and deep portions of the sediment bed, respectively (lower graph, Figure 4b). For consistency, E Profile model predictions are plotted against the same abscissa, $\sqrt{\bar{t}_\mathrm{C}}$, used for the C Profile model in Figure 4a. The experiment-specific transformation from $\bar{t}_\mathrm{C}$ to $\bar{t}_\mathrm{E}$ was determined by (1) fitting Equation 10a to Rhodamine WT concentration measured in the water column during experiment ID #20110613 (red points in Figure 4b, $a_\mathrm{E} = 50 \pm 1.2\ \mathrm{m}^{-1}$, $D_{\mathrm{eff},\,0}^\mathrm{E} = (5.6 \pm 0.5) \times 10^{-6}\ \mathrm{m}^2\ \mathrm{s}^{-1}$), and (2) substituting these inferred parameter values, together with experiment-specific values of the dimensionless water depth ($\bar{h}_w = a_\mathrm{E} h_w/\theta = 33 \pm 14$) and the C Profile's effective diffusivity ($D_{\mathrm{eff},\,0}^\mathrm{C} = (3.4 \pm 0.2) \times 10^{-7}\ \mathrm{m}^2\ \mathrm{s}^{-1}$), into the time transformation, $\bar{t}_\mathrm{E} = \left(\bar{h}_w^2 D_{\mathrm{eff},\,0}^\mathrm{E}/D_{\mathrm{eff},\,0}^\mathrm{C}\right)\bar{t}_\mathrm{C}$.

4.4. Experimental Evaluation of the C2E Profile

The C2E Profile's infinite bed model is a near-perfect representation of C16's water column measurements (top graph, Figure 4c). However, compared to the E Profile, the C2E infinite bed model systematically underestimates mixing in the streambed, especially at 15 mm below the SWI (compare lower graphs in Figures 4b and 4c). These model predictions were constructed by substituting the C2E's Green's function (Equations T4a–T4c in Table 1) into Equations 6a and 6b. C2E model predictions were then plotted against $\sqrt{\bar{t}_\mathrm{C}}$ following a modification of the two-step procedure outlined in section 4.3: (1) fitting the C2E model to Rhodamine WT concentration measured in the water column during experiment ID #20110613 ($D_{\mathrm{eff},\,0}^\mathrm{C2E} = (1.5 \pm 0.07) \times 10^{-6}\ \mathrm{m}^2\ \mathrm{s}^{-1}$, $\ell_t = 0.04 \pm 0.002$ m, $a_\mathrm{C2E} = 66 \pm 3.1\ \mathrm{m}^{-1}$); and (2) substituting these inferred values, along with experiment-specific values of the dimensionless water depth ($\bar{h}_w = a_\mathrm{C2E} h_w/\theta = 44 \pm 19$) and the C Profile's effective diffusivity ($D_{\mathrm{eff},\,0}^\mathrm{C} = (3.4 \pm 0.2) \times 10^{-7}\ \mathrm{m}^2\ \mathrm{s}^{-1}$), into the time transformation, $\bar{t}_\mathrm{C2E} = \left(\bar{h}_w^2 D_{\mathrm{eff},\,0}^\mathrm{C2E}/D_{\mathrm{eff},\,0}^\mathrm{C}\right)\bar{t}_\mathrm{C}$. The superscript or subscript "C2E" indicates the variables are specific to the C2E Profile.

5. Discussion

Here we discuss all 20 of C16's experiments, with the goal of answering the three questions raised in section 1.

5.1. How Is the Effective Diffusivity Structured Vertically?

C16's data set allows us to quantitatively compare the performance of the three diffusivity profiles (C, E, and C2E) over a permeability Reynolds number range (0.2–4.3) that spans dispersive mixing and turbulent diffusive regimes. Our earlier conclusion that the E Profile represents a substantial improvement over the C Profile (based on a comparison to Rhodamine WT measurements from Experiment ID #20110613, section 4) extends to the rest of C16's experiments as well (Figure 5). In all cases, the E Profile's infinite bed model captures a larger fraction of the variance in C16's water column measurements ($R^2 > 99.5\%$, Figure 5a) and has substantially smaller RMSE values (Figure 5b). The E Profile's AICc is also >10 units lower than the C Profile's AICc (Figure 5c) implying that the former model is preferred (Aho et al., 2014; Weijs & Ruddell, 2020).

The C2E Profile's infinite bed model also performs well. Compared to the E Profile, the C2E model has consistently lower RMSE and AICc values (compare crosses and red circles in Figures 5b and 5c) and a slightly improved coefficient of determination ($R^2 > 99.8\%$, Figure 5a). However, these improvements come at the

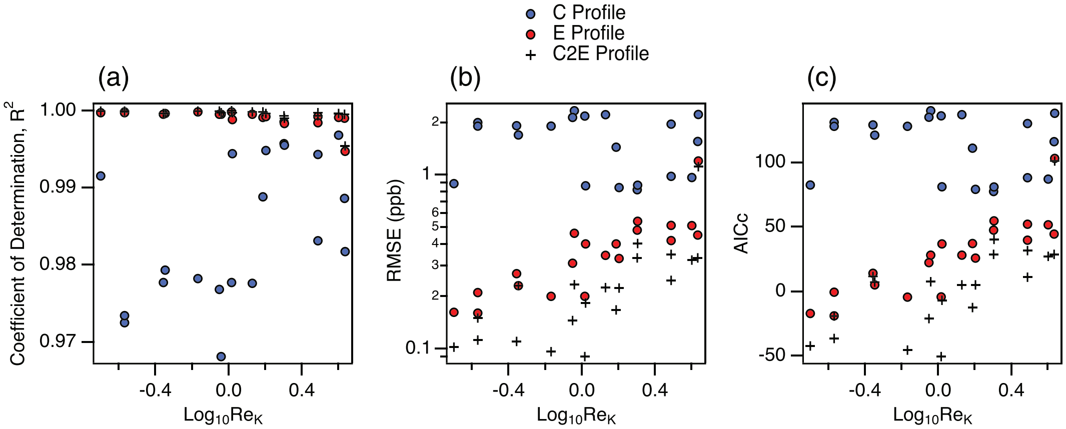

Figure 5. Performance of the C, E, and C2E infinite bed models across all 20 of Chandler et al.'s stirred tank experiments. Model performance metrics include (a) coefficient of determination, R^2; (b) root-mean-square error, RMSE; and (c) Akaike's information criterion, AICc.

cost of a new parameter (the C2E's inverse depth scale, a_{C2E}) whose inferred values are poorly constrained (coefficient of variation in excess of 40 for some experiments, see Table S7), highly variable (varying over 1,000-fold, Figure 6a) and, in some cases, not physically meaningful (e.g., the depth over which the effective diffusivity decays is $1/a_{\mathrm{C2E}} \approx 20$ μm for the largest value of a_{C2E} indicated in Figure 6a). Inferred values of the C2E Profile's other two parameters (effective diffusivity, $D_{\mathrm{eff},0}^{\mathrm{C2E}}$, and depth of constant mixing, ℓ_{t}) are strongly correlated ($R^2 = 0.93$ and 0.76) with the effective diffusivity, $D_{\mathrm{eff},0}^{\mathrm{E}}$, and decay scale, $1/a_{\mathrm{E}}$, inferred from the E Profile (Figures 6b and 6c). In summary, of the three profiles trialed in this study, the E Profile appears to be the most parsimonious description of the effective diffusivity's vertical structure.

5.2. Is the Flux Gradient Diffusive Model an Accurate Representation of Turbulent Solute Transport Through the Streambed?

While the E Profile's infinite bed model captures a large fraction of the variance in C16's water column measurements ($R^2 > 99.5\%$, Figure 5a), this assessment is based on the same data set that was used for model calibration. A more rigorous test can be stated as follows: Are the same E Profile parameter values obtained when the model is optimized with water column measurements versus when the model is optimized with sediment column measurements? Put another way, can the evolution of solute concentration in the interstitial fluid of the sediment bed be inferred from the evolution of solute concentration in the water column, and vice versa?

The answer is a qualified "yes." Effective diffusivities estimated from C16's water and sediment column data are strongly correlated over a 1,000-fold change in magnitude (Figure 7a, Pearson correlation coefficient, $R = 0.867$). Values of the inverse depth scale inferred from the water and sediment column data are much less variable and not significantly correlated (Figure 7b), but their respective log means ($a_{\mathrm{E}} = 10^{1.61 \pm 0.18}$ and $a_{\mathrm{E}} = 10^{1.70 \pm 0.08}$ m^{-1}, respectively) are equal within error (and consistent with the inverse depth scale reported by C16, $a = 55 = 10^{1.74}$ m^{-1}, estimated by dividing the sediment column into a series of layers and computing, with the C Profile model, diffusivities for each layer separately). This inverse depth scale corresponds to an "*e*-folding depth" (i.e., the depth at which the E Profile's effective diffusivity declines to $1/e \approx 0.37$ of its surficial value) of approximately 2 cm. This depth scale comports with previous field and laboratory estimates for the thickness of the benthic biolayer (2–5 cm) (Battin et al., 2008; Caruso et al., 2017; Dahm et al., 2002; Harvey et al., 2013; Kessler et al., 2013; Knapp et al., 2017; Krause et al., 2017; Tomasek et al., 2018; Trauth et al., 2014; Zarnetske et al., 2011). Hence, turbulent mixing may represent a universal mechanism for delivering the nutrients and energy needed for microbial growth in the benthic biolayer. More generally, the similar parameter values obtained from the water and sediment measurements support the claim that the gradient-flux diffusive model (Equation 1a) is a reasonable representation of turbulent solute transport across the SWI, provided that the diffusivity declines exponentially with depth into the streambed.

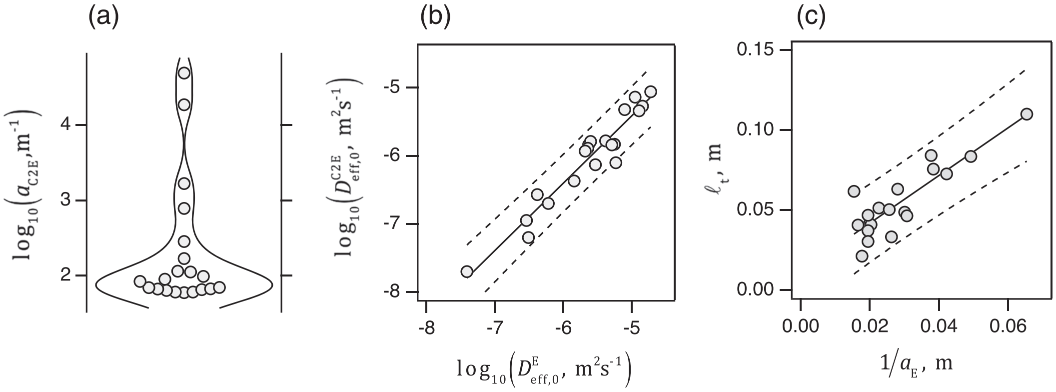

Figure 6. An evaluation of the C2E fitting parameters inferred from C16's water column data. (a) Values of the inverse decay-scale vary over 3 orders of magnitude, as illustrated here with a violin plot. The effective diffusivity (b) and depth of the constant mixing zone (c) inferred from the C2E profile model (vertical axes) are strongly correlated ($R^2 = 0.93$ and 0.76) with, respectively, the E Profile's effective diffusivity and inverse decay scale (horizontal axes) (dashed lines correspond to 95% prediction intervals).

While effective diffusivities inferred from data collected above and below the SWI are strongly correlated, some bias is evident when the permeability Reynolds number exceeds the threshold for a fully turbulent SWI, $Re_K > 2$ (Voermans et al., 2017) (Figure 7a). One possible explanation is C16's use of fluorometric measurements of tracer at a point in the sediment bed, which contrasts with the modeling assumption that solute concentrations are horizontally averaged (section 2). Chandler (2012) describes how measured concentration in the sediment was sensitive to fluorometer location and that these differences were consistent over time; that is, tracer appeared to mix out of the bed faster on one side of the tank than on the other (Chandler, 2012, p. 173). The authors also document distinct and persistent patterns of mean flow velocity within the tank (Chandler, 2012, p. 118), which would lead to heterogeneous turbulence intensities and corresponding heterogeneous efflux across the SWI at high permeability Reynolds numbers. To the extent that C16's point measurements are not equal to horizontally averaged concentrations, the effective diffusivities inferred from these data may be nonrepresentative. Indeed, Chandler (2012) noted an order of magnitude discrepancy in the time scale over which interstitial concentration declined on opposite sides of the stirred

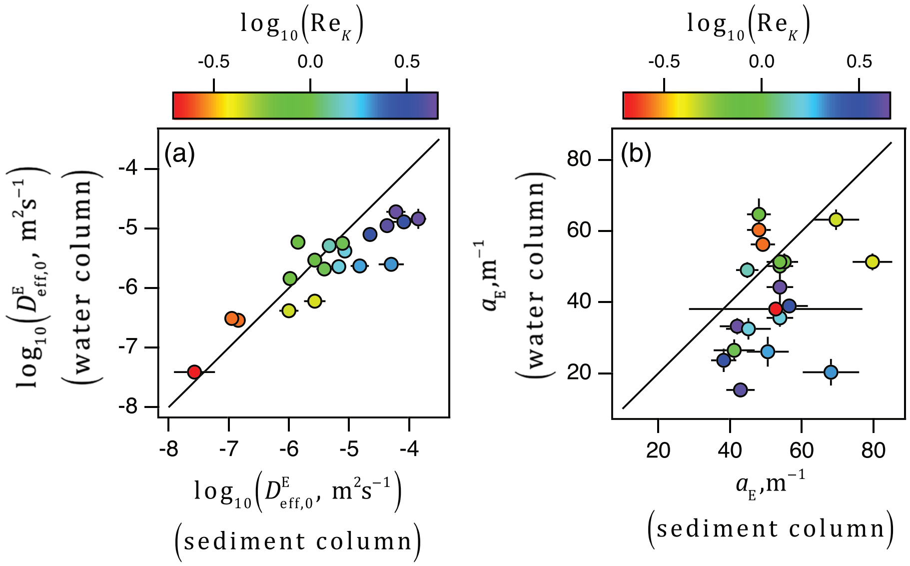

Figure 7. A comparison of (a) effective diffusivities and (b) inverse decay scales obtained by fitting the E Profile model to C16's water column (vertical axis) or sediment column (horizontal axis) data. The points are color coded to indicate the permeability Reynolds number.

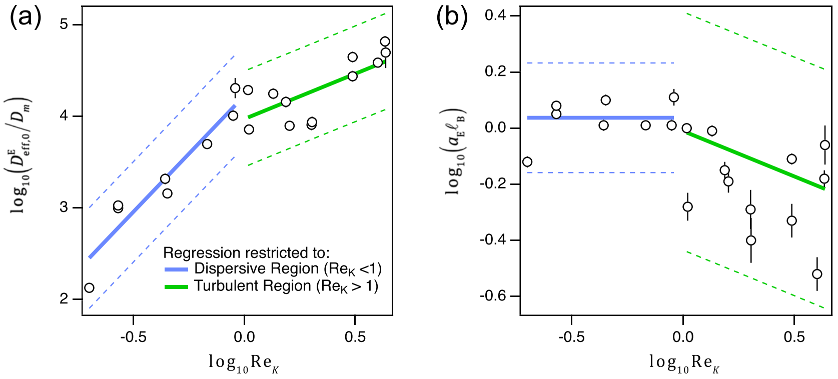

Figure 8. Permeability Reynolds number scaling of the E Profile's two parameters inferred from Chandler et al.'s water column measurements. The surficial diffusivity (a) and inverse decay-scale (b) follow different scaling behavior in the dispersive mixing (blue lines) and turbulent diffusive (green lines) ranges. Dashed lines are 95% prediction intervals.

tank—a discrepancy that could induce order-of-magnitude inaccuracy in estimated sediment side diffusivities (the scale of disagreement seen in Figure 7a for $Re_K > 2$).

An alternative explanation is that the flux gradient model (Equation 1a) is an imperfect descriptor of turbulent mass transfer through the sediment at high permeability Reynolds number—a conclusion supported by the slight reduction in E Profile model performance (i.e., higher RMSE and AICc values and lower R^2 values) with increasing permeability Reynolds number above, $Re_K > 2$ (Figure 5). The flux gradient description of dispersive mixing across other types of “porous” boundaries, such as vegetation canopies, is known to break down; for example, significant dispersive momentum flux can occur in regions of weak velocity gradient (Poggi & Katul, 2008), the analog of a concentration gradient for mass transfer. However, our estimates of diffusivity above and below the SWI in the dispersive regime ($0.01 < Re_K < 2$) are in general concordance (Figure 7a). It should also be noted, even at the highest permeability Reynolds numbers evaluated here, the flux gradient diffusive model still explains an overwhelming fraction of the variance in water concentration measurements ($R^2 > 0.995$)—provided that the diffusivity decays exponentially with depth (Figure 5a). Therefore, the flux gradient diffusive model is a reasonable representation of turbulent mass transfer in the interstitial fluids of the sediment bed, provided that the vertical structure of the effective diffusivity is correctly specified (e.g., with the E Profile).

5.3. Can Laboratory Measurements of Turbulent Mixing Across the SWI Be Extrapolated to Stream and Coastal Sediments?

Translation of our results to the field requires scaling relationships from which the E Profile's two parameters —the surficial effective diffusivity and inverse decay scale—can be estimated. Many studies have reported that effective diffusivities (inferred by fitting the C Profile's null model to flume measurements of turbulent mixing across flat sediment beds) exhibit a quadratic dependence on the permeability Reynolds number, $D^{\mathrm{C}}_{\mathrm{eff},\,0} \propto Re_K^2$ (Grant et al., 2012; O'Connor & Harvey, 2008; Richardson & Parr, 1988; Voermans et al., 2018). The permeability Reynolds number is calculated from the shear velocity, u_*, sediment bed permeability, K, and the kinematic viscosity of water, υ. Permeability can be estimated from the grain diameter and porosity of unconsolidated sediments (e.g., using the Kozeny-Carmen equation; Kamann et al., 2007) while the kinematic viscosity of water is determined primarily by temperature (Rumble, 2019). Several methods are available for measuring shear velocity (cf., Johnson & Cowen, 2017) including a force balance approach that provides a spatially averaged value from the stream's hydraulic radius (or depth, h_w, for wide streams) and slope, S (–): $u_* = \sqrt{gh_wS}$ where g is the gravitational acceleration. Thus, if the E Profile's two parameters can be expressed in terms of the permeability Reynolds number, such relationships would allow translation of laboratory measurements to field applications.

When our inferred effective diffusivities are plotted against the permeability Reynolds number, a significant change in slope and intercept (as represented by nonoverlapping 95% confidence intervals) is evident around $Re_K = 1$ (Figure 8a):

$$\log_{10}\frac{D^{\mathrm{E}}_{\mathrm{eff},\,0}}{D_m} = \begin{cases} (4.22\pm0.09)+(2.53\pm0.17)\times\log_{10}Re_K,\ R^2=0.905,\ Re_K<1 \\ (3.97\pm0.06)+(0.99\pm0.15)\times\log_{10}Re_K,\ R^2=0.440,\ Re_K>1 \end{cases} \tag{11a}$$

The power law exponent for the surficial effective diffusivity spans the quadratic dependence noted above, declining from 2.53 ± 0.17 in the dispersive mixing regime ($Re_K < 1$) to 0.99 ± 0.15 in the turbulent diffusive regime ($Re_K > 1$). Note that this scaling relationship is normalized by the molecular diffusion coefficient for Rhodamine WT in water at 21°C ($D_m = 2.9 \times 10^{-10}\ \mathrm{m^2 s^{-1}}$) (Chandler, 2012). Therefore, over the range of permeability Reynolds number captured in C16's study, turbulence enhances mixing by 10^2 to 10^5 above that expected for molecular diffusion alone (Figure 8a).

Equation 11b is our scaling relationship for the E Profile's inverse decay scale, here normalized by a rough estimate for the thickness of the benthic biolayer (Knapp et al., 2017): $\ell_{\mathrm{B}} = 2$ cm (Figure 8b).

$$\log_{10}a_{\mathrm{E}}\ell_{\mathrm{B}} = \begin{cases} 0.04\pm0.01,\ Re_K<1 \\ (0\pm0.02)-(0.32\pm0.08)\times\log_{10}Re_K,\ R^2=0.18,\ Re_K>1 \end{cases} \tag{11b}$$

The implied turbulent mixing depth ($1/a_{\mathrm{E}}$) transitions from being roughly equal to the benthic biolayer thickness in the dispersive mixing regime ($Re_K < 1$, $1/a_{\mathrm{E}} \approx \ell_{\mathrm{B}}$) to a weak inverse dependence on the permeability Reynolds number in the turbulent diffusive regime ($Re_K > 1, a_{\mathrm{E}}\ell_{\mathrm{B}} \propto Re_K^{-0.32\,\pm\,0.08}$). The minimum turbulent mixing depth, $1/a_{\mathrm{E}} \geq \ell_{\mathrm{B}} \approx 2$ cm, is between 4 and 130 times the diameter of the glass spheres that make up the sediment bed ($0.150 \leq d_g \leq 5$ mm) and about 20 times the estimated thickness of the Brinkman Layer (the region of enhanced mean velocity at the top of the sediment) $\delta_b \approx 20\sqrt{K} = 0.9$ mm (Voermans et al., 2017). It is also about tenfold less than the sediment bed depth ($d_b = 20$ cm), implying that $1/a_{\mathrm{E}}$ is not a proxy for bed depth. These comparisons raise the following question: What is the physical interpretation of the inverse decay scale?

Based on a model for mass exchange across the SWI by turbulent dispersive mixing, Higashino et al. (2009) reported that, at depths of around 2 cm and for shear velocities on the lower end of the range employed by C16, the root-mean-square vertical velocity of the interstitial pore fluids are >10% of their value at the SWI (Higashino et al., 2009; Figure 3). Thus, when $Re_K < 1$, the inverse decay scale likely represents the surficial depth over which mass is vigorously mixed by turbulence-induced dispersive mixing. This physical interpretation of a_{E}^{-1} also holds for cases when turbulent diffusion controls solute transport (i.e., $Re_K > 1$). In this regime, regions of the streambed where solute is rapidly mixed correspond to regions of elevated turbulent shear stresses (Roche et al., 2018). Because turbulent shear stresses propagate deeper into the streambed at elevated Re_K (Voermans et al., 2017), rapid solute mixing is expected to extend deeper into the streambed as Re_K increases. This expectation is in direct agreement with our observations of a_{E} decreasing with Re_K when $Re_K > 1$ (Figure 8b).

Because the above scaling relationships (Equations 11a and 11b) are based on C16's stirred tank experiments, they may not apply to all turbulent environmental flows. For example, while C16's permeability Reynolds number range includes dispersive mixing and turbulent diffusive regimes, their shear velocities are on the low side ($u_* = 0.01$ to $0.04\ \mathrm{m\ s^{-1}}$) for headwater streams (Hall et al., 2009). Field validation of Equations 11a and 11b will be an important next step.

6. Conclusions

In this paper, we developed and tested a rigorous one-dimensional modeling framework, based on Duhamel's Theorem, for predicting mass transfer across the SWI and through the benthic biolayer of a turbulent stream. The framework allows for depth-varying diffusivity profiles and encodes two-way coupling across the SWI. The theory is applied to previously published measurements of turbulent mixing across a flat sediment bed in a stirred tank (Chandler et al., 2016) to evaluate the performance of three diffusivity depth profiles (C, E, and C2E Profiles). Key findings include (1) the flux gradient diffusive model is a reasonable representation of turbulent mass transfer across the SWI and in the sediment bed, provided that the vertical structure of the effective diffusivity is correctly specified; (2) The experimental data are consistent with an exponentially declining diffusivity profile (i.e., the E Profile); (3) values of the E Profile's two parameters (surficial effective diffusivity at the SWI, $D^{\mathrm{E}}_{\mathrm{eff},0}$, and decay depth scale, a_{E}) vary with the permeability Reynolds number, Re_K, providing a direct link between lab results and field-scale applications; (4) the E Profile's dependence on the permeability Reynolds number changes abruptly at $Re_K = 1$, reflecting different modes of mixing below (turbulent dispersive mixing) and above (turbulent diffusion) this threshold; and (5) the effective diffusivity's e-folding depth is concordant with field and laboratory measurements of the benthic biolayer thickness. Therefore, turbulent mixing across the SWI may serve as a universal transport mechanism, supplying the nutrient and energy fluxes needed to sustain microbial growth, and nutrient processing, in the benthic biolayer of stream and coastal sediments.

Conflict of Interest

The authors declare no conflicts of interest.

Data Availability Statement

All data used in this study are publicly available (www.doi.org/10.15131/shef.data.10120205).

Acknowledgments

S. B. G. was supported by the U.S. National Science Foundation (Awards 1840504 and 2021015), Virginia Tech's ICTAS EFO Opportunity Seed Investment Grant, and the UC Office of the President Multicampus Research Program Initiative award (MRP-17-455083). J. G. V. was funded by the U.S. National Science Foundation (Award EAR 1830172) and the U.S. Department of Energy, Office of Biological and Environmental Research (BER), as part of BER's Subsurface Biogeochemistry Research Program (SBR). This contribution originates from the SBR Scientific Focus Area (SFA) at the Pacific Northwest National Laboratory (PNNL). I. G. was supported by UK EPSRC Established Career Fellowship (Award EP/P012027/1). M. G. was funded by an Australian Research Council Discovery Project (DP120102500). K. R. R. was supported by the Fulbright program. J. H. was supported by the U.S. Geological Survey Water Availability and Use Science Program. Supporting Information includes tables and text. The authors thank M. Chappell, A. Monofy, three anonymous reviewers, and the Associate Editor for their insightful comments and manuscript edits. Any use of trade, firm, or product names is for descriptive purposes only and does not imply endorsement by the U.S. Government.

References

Aho, K., Derryberry, D., & Peterson, T. (2014). Model selection for ecologists: The worldviews of AIC and BIC. *Ecology*, *95*(3), 631–636. https://doi.org/10.1890/13-1452.1

Azizian, M., Boano, F., Cook, P. L. M., Detwiler, R. L., Rippy, M. A., & Grant, S. B. (2017). Ambient groundwater flow diminishes nitrate processing in the hyporheic zone of streams. *Water Resources Research*, *53*, 3941–3967. https://doi.org/10.1002/2016WR020048

Battin, T. J., Kaplan, L. A., Findlay, S., Hopkinson, C. S., Marti, E., Packman, A. I., et al. (2008). Biophysical controls on organic carbon fluxes in fluvial networks. *Nature Geoscience*, *1*(2), 95–100. https://doi.org/10.1038/ngeo101

Boano, F., Harvey, J. W., Marion, A., Packman, A. I., Revelli, R., Ridolfi, L., & Wörman, A. (2014). Hyporheic flow and transport processes: Mechanisms, models, and biogeochemical implications. *Reviews of Geophysics*, *52*, 603–679. https://doi.org/10.1002/2012RG000417

Boano, F., Revelli, R., & Ridolfi, L. (2011). Water and solute exchange through flat streambeds induced by large turbulent eddies. *Journal of Hydrology*, *402*(3–4), 290–296. https://doi.org/10.1016/j.jhydrol.2011.03.023

Bottacin-Busolin, A. (2019). Modeling the effect of hyporheic mixing on stream solute transport. *Water Resource Research*, *55*, 9995–10011. https://doi.org/10.1029/2019WR025697

Breugem, W. P., Boersma, B. J., & Uittenbogaard, R. E. (2006). The influence of wall permeability on turbulent channel flow. *Journal of Fluid Mechanics*, *562*, 35–72. https://doi.org/10.1017/S0022112006000887

Cardenas, M., Wilson, J. L., & Haggerty, R. (2008). Residence time of bedform-driven hyporheic exchange. *Advances Water Research*, *31*(10), 1382–1386. https://doi.org/10.1016/j.advwatres.2008.07.006

Caruso, A., Boano, F., Ridolfi, L., Chopp, D. L., & Packman, A. (2017). Biofilm-induced bioclogging produces sharp interfaces in hyporheic flow, redox conditions, and microbial community structure. *Geophysical Research Letters*, *44*, 4917–4925. https://doi.org/10.1002/2017GL073651

Chandler, I. D. (2012). *Vertical variation in diffusion coefficient within sediments* (PhD thesis). Coventry, UK: University of Warwick.

Chandler, I. D., Guymer, I., Pearson, J. M., & Egmond, R. V. (2016). Vertical variation of mixing within porous sediment beds below turbulent flows. *Water resources research*, *52*, 3493–3509. doi.org/10.1002/2015WR018274

Dahm, C. N., Grimm, N. B., Marmonier, P., Valett, H. M., & Vervier, P. (2002). Nutrient dynamics at the interface between surface waters and groundwaters. *Freshwater Biology*, *40*(3), 427–451. https://doi.org/10.1046/j.1365-2427.1998.00367.x

Elliott, A. H., & Brooks, N. H. (1997a). Transfer of nonsorbing solutes to a streambed with bed forms: Theory. *Water Resources Research*, *33*, 123–136. https://doi.org/10.1029/96WR02784

Elliott, A. H., & Brooks, N. H. (1997b). Transfer of nonsorbing solutes to a streambed with bed forms: Laboratory experiments. *Water Resources Research*, *33*, 137–151. https://doi.org/10.1029/96WR02783

Fleckenstein, J. H., Krause, S., Hannah, D. M., & Boano, F. (2010). Groundwater-surface water interactions: New methods and models to improve understanding of processes and dynamics. *Advances in Water Resources*, *33*(11), 1291–1295. https://doi.org/10.1016/j.advwatres.2010.09.011

Franca, M. J., & Brocchini, M. (2015). Turbulence in rivers. In P. Rowinski, & A. Radecki-Pawlick (Eds.), *Rivers—Physical, fluvial, and environmental processes, GeoPlanet: Earth and planetary sciences* (pp. 51–78). Switzerland: Springer international publishing. https://doi.org/10.1007/978030319-17719-9_2

Graf, U. (2004). *Applied Laplace transforms and z-transforms for scientists and engineers—A computational approach using a Mathematica package* (1st ed.). New York, NY: Springer-Basal AG.

Grant, S. B., Azizian, M., Cook, P., Boano, F., & Rippy, M. A. (2018). Factoring stream turbulence into global assessments of nitrogen pollution. *Science*, *359*(6381), 1266–1269. https://doi.org/10.1126/science.aap8074

Grant, S. B., Gomez-Velez, J. D., & Ghisalberti, M. (2018). Modeling the effects of turbulence on hyporheic exchange and local-to-global nutrient processing in streams. *Water Resources Research*, *54*, 5883–5889. https://doi.org/10.1029/2018WR023078

Grant, S. B., & Marusic, I. (2011). Crossing turbulent boundaries: Interfacial flux in environmental flows. *Environmental Science and Technology*, *45*, 7107–7113. https://doi.org/10.1021/es201778s

Grant, S. B., Monofy, A., Boano, F., Gomez-Velez, J. D., Guymer, I., Harvey, J., & Ghisalberti, M. (2020). Unifying advective and diffusive descriptions of bedform pumping in the benthic biolayer of streams. *Water Resources Research*. e2020WR027967. https://doi.org/10.1029/2020wr027967

Grant, S. B., Stewardson, M. J., & Marusic, I. (2012). Effective diffusivity and mass flux across the sediment-water interface in streams. *Water Resources Research*, *48*, W05548. https://doi.org/10.1029/2011WR011148

Grant, S. B., Stolzenbach, K., Azizian, M., Stewardson, M. J., Boano, F., & Bardini, L. (2014). First-order contaminant removal in the hyporheic zone of streams: Physical insights from a simple analytical model. *Environmental Science and Technology*, *48*(19), 11,369–11,378. https://doi.org/10.1021/es501694k

Hall, R. O., Tank, J. L., Sobata, D. J., Mulholland, P. J., O'Brien, J. M., Dodds, W. K., et al. (2009). Nitrate removal in stream ecosystems measured by ^{15}N addition experiments: Total uptake. *Limnology and Oceanography*, *43*, 653–665.

Harvey, J. W., Böhlke, J. K., Voytek, M. A., Scott, D., & Tobias, C. R. (2013). Hyporheic zone denitrification: Controls on effective reaction depth and contribution to whole-stream mass balance. *Water Resources Research*, *49*, 6298–6316. https://doi.org/10.1002/wrcr.20492

Herzog, S. P., Higgins, C. P., Singha, K., & McCray, J. E. (2018). Performance of engineered streambeds for inducing hyporheic transient storage and attenuation of resazurin. *Environmental Science & Technology*, *52*, 10,627–10,636. https://doi.org/10.1021/acs.est.8b01145

Hester, E. T., Cardenas, M. B., Haggerty, R., & Apte, S. V. (2017). The importance and challenge of hyporheic mixing. *Water Resources Research*, *53*, 3565–3575. https://doi.org/10.1002/2016WR020005

Higashino, M. J., Clark, J., & Stefan, H. (2009). Pore water flow due to nearbed turbulence and associated solute transfer in a stream or lake sediment bed. *Water Resources Research*, *45*, W12414. https://doi.org/10.1029/2008WR007374

Hondzo, M. (1998). Dissolved oxygen transfer at the sediment-water interface in a turbulent flow. *Water Resources Research*, *34*(12), 3525–3533. https://doi.org/10.1029/1998WR900009

Incropera, F. P., Dewitt, D. P., Bergman, T. L., & Lavine, A. S. (2007). *Fundamentals of heat and mass transfer*. Hoboken, NJ: John Wiley.

Johnson, E. D., & Cowen, E. A. (2017). Estimating bed shear stress from remotely measured surface turbulent dissipation fields in open channel flows. *Water Resources Research*, *53*, 1982–1996. https://doi.org/10.1002/2016WR018898

Kamann, P. J., Ritzi, R. W., Dominic, D. F., & Conrad, C. M. (2007). Porosity and permeability in sediment mixtures. *Ground Water*, *45*(4), 429–438. https://doi.org/10.1111/j.1745-6584.2007.00313.x

Kessler, A. J., Glud, R. N., Cardenas, M. B., & Cook, P. L. M. (2013). Transport zonation limits coupled nitrification-denitrification in permeable sediments. *Environmental Science and Technology*, *47*(23), 13,404–13,411. https://doi.org/10.1021/es403318x

Kim, T., Blois, G., Best, J., & Christensen, K. (2020). Experimental evidence of amplitude modulation in permeable-wall turbulence. *Journal of Fluid Mechanics*, *887*, A3. https://doi.org/10.1017/jfm.2019.1027

Knapp, J. L., González-Pinzón, R., Drummond, J. D., Larsen, L. G., Cirpka, O. A., & Harvey, J. W. (2017). Tracer-based characterization of hyporheic exchange and benthic biolayers in streams. *Water Resources Research*, *53*, 1575–1594. https://doi.org/10.1002/2016WR019393

Krause, S., Lewandowski, J., Grimm, N. B., Hannah, D. M., Pinay, G., McDonald, K., et al. (2017). Ecohydrological interfaces as hot spots of ecosystem processes. *Water Resources Research*, *53*, 6359–6376. https://doi.org/10.1002/2016WR019516

Laube, G., Schmidt, C., & Fleckenstein, J. H. (2018). The systematic effect of streambed conductivity heterogeneity on hyporheic flux and residence time. *Advances Water Research*, *122*, 60–69. https://doi.org/10.1016/j.advwatres.2018.10.003

Leij, F. J., Priesack, E., & Schaap, M. G. (2000). Solute transport modeled with Green's functions with application to persistent solute sources. J. *Contaminant Hydrology*, *41*, 155–173. https://doi.org/10.1016/S0169-7722(99)00062-5

Marion, A., & Zaramella, M. (2015). Diffusive behavior of bedform-induced hyporheic exchange in rivers. *Journal of Environmental Engineering*, *131*(9), 1260–1266. https://doi.org/10.1061/(ASCE)0733-9372(2005)131:9(1260)

Myers, G. E. (1971). *Analytical methods in conduction heat transfer*. New York: McGraw-Hill.

Nagaoka, H., & Ohgaki, S. (1990). Mass transfer mechanism in a porous riverbed. *Water Research*, *24*(4), 417–425. https://doi.org/10.1016/0043-1354(90)90223-S

Newcomer, M. E., Hubbard, S. S., Fleckenstein, J. H., Maier, U., Schmidt, C., Thullner, M., et al. (2016). Simulating bioclogging effects on dynamic riverbed permeability and infiltration. *Water resources research*, *52*(4), 2883–2900. https://doi.org/10.1002/2015WR018351

O'Connor, B. L., & Harvey, J. W. (2008). Scaling hyporheic exchange and its influence on biogeochemical reactions in aquatic ecosystems. *Water Resources Research*, *44*, W12423. https://doi.org/10.1029/2008WR007160

O'Connor, B. L., & Hondzo, M. (2008). Dissolved oxygen transfer to sediments by sweep and eject motions in aquatic environments. *Limnology and Oceanography*, *53*(2), 566–578. https://doi.org/10.4319/lo.2008.53.2.0566

Packman, A. I., Salehin, M., & Zaramella, M. (2004). Hyporheic exchange with gravel beds: Basic hydrodynamic interactions and bedform-induced advective flows. *ASCE J. Hydraulic Engineeering.*, *130*(7), 647–656. https://doi.org/10.1061/(ASCE)0733-9429(2004)130:7(647)

Perez Guerrero, J. S., Pontedeiro, E. M., van Genuchten, M. T., & Skaggs, T. H. (2013). Analytical solutions of the one-dimensional advection-dispersion solute transport equation subject to time-dependent boundary conditions. *Chemical Engineering Journal*, *221*, 487–491. https://doi.org/10.1016/j.cej.2013.01.095

Poggi, D., & Katul, G. G. (2008). Micro- and macro-dispersive fluxes in canopy flows. *Acta Geophysica*, *56*(3), 778–799. https://doi.org/10.2478/s11600-008-0029-7

Pokrajac, D., & Manes, C. (2009). Velocity measurements of a free-surface turbulent flow penetrating a porous medium composed of uniform-size spheres. *Transport in porous media*, *78*(3), 367–383. https://doi.org/10.1007/s11242-009-9339-8

Reidenbach, M. A., Limm, M., Hondzo, M., & Stacey, M. T. (2010). Effects of bed roughness on boundary layer mixing and mass flux across the sediment-water interface. *Water Resources Research*, *46*, W07530. https://doi.org/10.1029/2009WR008248

Richardson, C. P., & Parr, A. D. (1988). Modified Fickian model for solute uptake by runoff. ASCE J. *Environmental Engineering*, *114*(4), 792–809. https://doi.org/10.1061/(ASCE)0733-9372(1988)114:4(792)

Roche, K. R., Blois, G., Best, J. L., Christensen, K. T., Aubeneau, A. F., & Packman, A. I. (2018). Turbulence links momentum and solute exchange in coarse-grained streambeds. *Water Resources Research*, *54*, 3225–3242. https://doi.org/10.1029/2017WR021992

Roche, K. R., Li, A., Bolster, D., Wagner, G. J., & Packman, A. I. (2019). Effects of turbulent hyporheic mixing on reach-scale transport. *Water Resources Research*, *55*, 3780–3795. https://doi.org/10.1029/2018WR023421

Rumble, J. (Ed.). (2019). *CRC handbook of chemistry and physics* (100th ed.). Boca Rotan, FL: CRC Press, Taylor and Francis Group.

Salehin, M., Packman, A. I., & Paradis, M. (2004). Hyporheic exchange with heterogeneous streambeds: Laboratory experiments and modeling. *Water Resources Research*, *40*, W11504. https://doi.org/10.1029/2003wr002567

Stewardson, M. J., Datry, T., Lamouroux, N., Pella, H., Thommeret, N., Valette, L., & Grant, S. B. (2016). Variation in reach-scale hydraulic conductivity of streambeds. *Geomorphology*, *259*, 70–80. https://doi.org/10.1016/j.geomorph.2016.02.001

Thibodeaux, L. J., & Boyle, J. D. (1987). Bedform-generated convective transport in bottom sediment. *Nature*, *325*(6102), 341–343. https://doi.org/10.1038/325341a0

Thibodeaux, L. J., Matisoff, G., & Reible, D. D. (2011). Bioturbation and other sorbed-phase transport processes in surface soils and sediments. In L. J. Thibodeaux & D. Mackay (Eds.), *Handbook of chemical mass transport in the environment* (Chap. 13, pp. 369–383). Boca Raton, FL: CRC Press, Taylor and Francis Group.

Tomasek, A. A., Barman, T. D., Wang, P., Kozarek, J. L., Staley, C., Sadowsky, M. J., & Hondzo, M. (2018). The effects of turbulence and carbon amendments on nitrate uptake and microbial gene abundances in stream sediment. *Journal Geophysical Research: Biogeoscience*, *123*, 1289–1301. https://doi.org/10.1002/2017JG004261

Trauth, N., Schmidt, C., Vieweg, M., Maier, U., & Fleckenstein, J. H. (2014). Hyporheic transport and biogeochemical reactions in pool-riffle systems under varying ambient groundwater flow conditions. *Journal Geophysical Research: Biogeosciences*, *119*, 910–928. https://doi.org/10.1002/2013JG002586

Voermans, J. J., Ghisalberti, M., & Ivey, G. N. (2017). The variation of flow and turbulence across the sediment-water interface. *Journal of Fluid Mechanics*, *824*, 413–437. https://doi.org/10.1017/jfm.2017.345

Voermans, J. J., Ghisalberti, M., & Ivey, G. N. (2018). A model for mass transport across the sediment-water interface. *Water Resources Research*, *54*, 2799–2812. https://doi.org/10.1002/2017WR022418

Weijs, S. V., & Ruddell, B. L. (2020). Debates: Does information theory provide a new paradigm for earth science? Sharper predictions using Occam's digital razor. *Water resources research*, *56*, e2019Wr026471. https://doi.org/10.1029/2019WR026471

Wolke, P., Teitelbaum, Y., Deng, C., Lewandowski, J., & Arnon, S. (2020). Impact of bed form celerity on oxygen dynamics in the hyporheic zone. *Water*, *12*, 62. https://doi.org/10.3390/w12010062

Wörman, A. (2000). Comparison of models for transient storage of solutes in small streams. *Water Resources Research*, *36*(2), 455–468. https://doi.org/10.1029/1999WR900281

Zarnetske, J. P., Haggerty, R., Wondzell, S. M., & Baker, M. A. (2011). Dynamics of nitrate production and removal as a function of residence time in the hyporheic zone. *Journal of Geophysical Research*, *116*, G01025. https://doi.org/10.1029/2010JG001356

Zheng, L., Cardenas, M. B., Wang, L., & Mohrig, D. (2019). Ripple effects: Bedform morphodynamics cascading into hyporheic zone biogeochemistry. *Water Resources Research*, Advanced online publication, *55*, 7320–7342. https://doi.org/10.1029/29018WR023517

Zhong, Q., Chen, Q., Wang, H., Li, D., & Wang, X. (2016). Statistical analysis of turbulent super-streamwise vortices based on observations of streaky structures near the free surface in the smooth open channel flow. *Water Resources Research*, *52*, 3563–3578. https://doi.org/10.1002/2015WR017728